Automated geometric reconstruction and cable force inference for cable-net structures using 3D point clouds

Siwei Lin [b], Liping Duan [a,b,c], Jiming Liu [b], Xiao Xiao [a,b,c], Ji Miao [b], Jincheng Zhao [a,b,c,*]

[a] *State Key Laboratory of Ocean Engineering, School of Ocean and Civil Engineering, Shanghai Jiao Tong University, Shanghai 200240, China*
[b] *School of Ocean and Civil Engineering, Shanghai Jiao Tong University, Shanghai, China*
[c] *Shanghai Key Laboratory for Digital Maintenance of Buildings and Infrastructure, Department of Civil Engineering, Shanghai Jiao Tong University, Shanghai, China*

A R T I C L E   I N F O

A B S T R A C T

Laser scanning provides an efficient solution to digital twin construction in civil engineering. The complexity and redundancy of large-scale point clouds substantially prolong the labor-intensive model reconstruction process. This paper presents an automated and high-precision geometric reconstruction approach for cable-net structures with a complete workflow from raw points to the extraction of cable shapes and forces. The strategy involves the extraction of coordinates of key cable regions through the characterization of cable geometry and local registration methods, followed by the computation of cable forces and shapes using segmented catenary theory and nonlinear optimization. The approach is validated with a single-curvature cable-net structure, with the accuracy of cable shapes within ± 5 mm and errors in cable forces $<5\%$. The method contributes to health monitoring and rapid reconstruction of cable-net structures. The precise geometry and forces will facilitate the creation of the mechanical models reflecting the physical authenticity of structures.

1. Introduction

As a type of spatial structures widely adopted in large-span infrastructure, cable-net structures undergo large geometric variations in the construction process, necessitating real-time monitoring of cable forces and shapes for construction safety. The digital twin of a structure reflects the structural behavior in a timely manner based on the historical data, the real-time sensor data and the physical modeling [1], which is a promising technology for enhancing construction productivity and ensuring structural safety throughout the life cycle of the structure. A high-fidelity 3D geometric model is fundamental to the digital twin, as it is essential for other functional components in the twin model, such as numerical analysis and visualization. However, the digital twinning of cable-net structures faces special challenges due to the geometric complexity of the construction process. With the advancements in computer vision, 3D point clouds have become a prevalent geometric representations for reconstruction purposes [2]. Compared to the labor-intensive single-point measurement, 3D laser scanning offers high precision and efficiency in obtaining big point cloud data. Nonetheless, challenges such as noise, occlusion and the insufficient amount of data pose significant obstacles to the geometric reconstruction of cable-net structures.

In this paper, we propose an automated approach specifically for cable nets, aiming to extract cable shapes and forces from scanned point clouds. The proposed method streamlines the extraction process by automatically extracting the cable forces and precisely determining the cable net shapes. The efficiency and fidelity in geometric extraction of this method are beneficial to the realization of digital twins. The framework of the approach is illustrated in Fig. 1. Employing a divide and conquer strategy, the points of each cable are first segmented from the cable-net based on the geometric features of cables. This segmentation reduces computational costs compared with processing the raw point cloud as a whole. Subsequently, crucial position information of the cable, including coordinates of the cable axis, anchorage points and concentrated loading, is obtained efficiently and automatically using three proposed processing methods. Afterwards, cable shapes and cable forces are computed based on the segmental catenary theory. The automated approach exhibits notable advantages in efficiently and robustly handling large-scale cable-net point clouds containing complex scanned data, including occlusions, non-uniformity and noise. The approach adheres to the assumptions of catenary theory: (1) the cable material is linearly elastic and abides by Hooke's Law; (2) the cable is
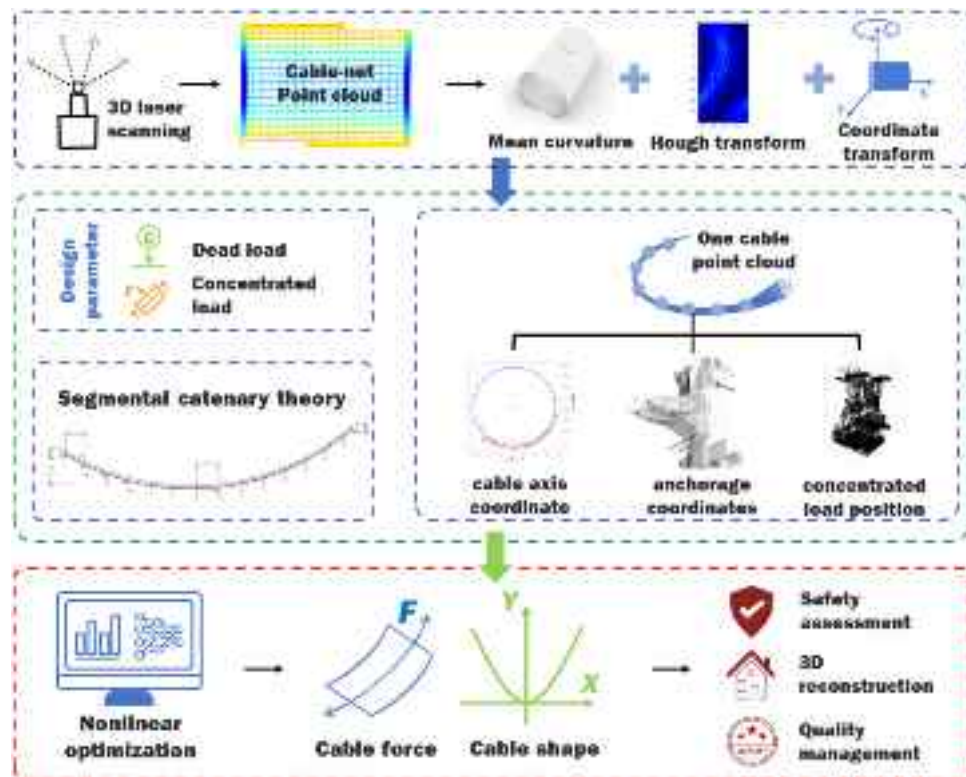
Fig. 1. Framework of the proposed approach based on 3D point clouds.

treated as ideally flexible and can only sustain tension, neglecting the influence of the cross-sectional bending stiffness on the cable shape; (3) the change in the cross-sectional area of the cable before and after deformation is disregarded; (4) horizontal deformation of the cable is considered negligible.

The rest of this paper is organized as follows. Section 2 presents a literature review on geometric representation extraction and object recognition. In Section 3, the framework of the methodology is described in detail. The proposed approach is validated with a scanned point cloud of a real cable-net structure during the construction phase in Section 4. Finally, conclusions and future work are discussed in Section 5.

2. Literature review

2.1. Methods of acquiring geometric representations
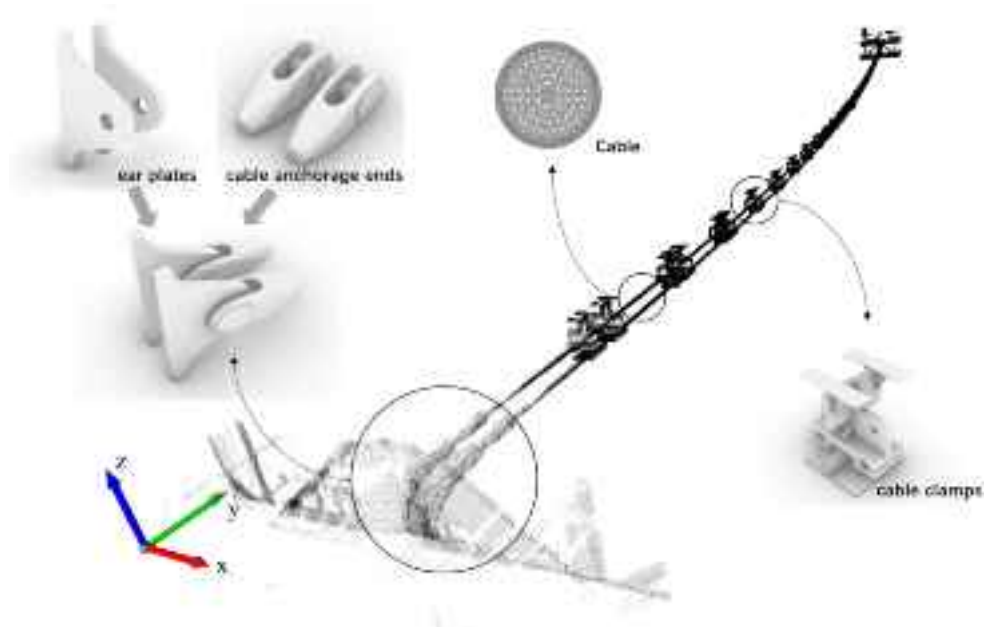
When it comes to acquiring geometric representations of large-scale scenes, two methods are widely used, i.e., laser scanning and oblique photography. Terrestrial laser scanning offers scanning accuracy and resolution at the millimeter level, but it may face limitations due to terrain constraints and susceptibility to occlusion. With the development of consumer-grade drones, oblique photography has emerged as an alternative method for 3D modeling [3,4]. Leveraging the mobility and flexibility of drones, oblique photography offers advantage of effectively avoiding occlusion issues. However, it may come with a trade-off of reduced scanning accuracy and resolution, typically operating at the centimeter level [5]. Some research efforts have combined laser scanning and oblique photography to maximize geometric information in buildings, particularly in modeling historical structures and bridges [6,7].

In the context of acquiring geometric information for the cable-net structure studied in this paper, the terrestrial laser scanning is preferred due to its ability to provide high accuracy and resolution. Given that the diameters of cables are usually in the range of 50-100

mm, using oblique photography could result in the loss of significant geometric details of the cables, affecting the accuracy of cable shape extraction and tension estimation. Additionally, most components of the cable net have conventional geometric shapes, making them less sensitive to occlusion. As a result, crucial geometric information pertaining to the cable net can be effectively extracted from existing laser scanning data.

2.2. Geometric representation extraction from point cloud

Geometric fitting techniques such as slicing and skeletonization of point clouds have been widely employed for slender members, where the axis represents the primary geometry. The advantage of these techniques lies in dimension reduction to enhance the processing efficiency and fitting accuracy. Hough transform [8], random sample consensus [9] and least square fitting [10] are commonly applied to fit cross-sections with simple geometric features such as lines, circles and planes. More complex cross-sections are addressed using the kernel density [11] and the image convolution [12] applied to sliced point cloud data. At the component level, it is primary to use point cloud slicing and skeleton extraction for geometric extraction of the components, enabling various applications such as initial imperfection extraction [10,13,14], buckling behavior analysis [15] and geometric detection [16,17]. At the structure level, this method is applied in the reconstruction for steel frames [12,18], main cables of suspension bridges [9], steel girder bridges [19] and cylindrical MEP (Mechanical, Electrical, Plumbing) components [8,20]. For members with general shapes, the geometric fitting often employs constructive solid geometry (CSG) [21] or boundary representation (B-rep). NURBS (Non-Uniform Rational B-Splines) [22] have gained popularity in B-rep methods due to their flexibility and accuracy in geometry control. Andrey Dimitrov et al. [23] leverages the segmented point cloud and NURBS surface fitting for the geometric reconstruction of pipelines. Andrea Ursini et al. [24] reconstructed the roof models of complex historical buildings with NURBS surface fitting. Christopher Rausch et al. [25] extracted the

Fig. 2. Point cloud of an entire cable consisting of cable clamps, the cable body and the anchorage.

parameterized data of CSG and B-rep descriptions from the BIM model. By utilizing metaheuristic algorithms, the parameterized data was iteratively updated to achieve alignment between geometric shapes and point clouds. This process ultimately led to the updating of the geometric shape and pose of the BIM model. Nevertheless, a major challenge in geometric representation extraction is the significant influence of point cloud density and occlusion on the quality of geometric reconstruction. Moreover, the unordered nature of raw data underscores the importance of object recognition in large-scale point clouds for accurate geometric reconstruction.

2.3. Object recognition and segmentation

In simple scenarios, object recognition and segmentation can be accomplished by single method, such as region growing method or surface normal analysis. For more intricate scenes, advanced techniques and algorithms are necessary to fulfill the recognition tasks, e.g. the contextual relationships, local descriptors, model-driven and semantic segmentation. The surface features (e.g., size, position, orientation, topology, etc.) [26] and contextual relationships [27] are utilized to automatically segment the point cloud into different parts, such as walls, ceilings and floors. Various local feature descriptors have been proposed for the registration and recognition of 3D objects [28,29]. CAD and BIM models often serve as references for matching point clouds to structures. Changmin Kim et al. [30,31] and Frédéric Bosché et al. [32] have converted CAD and BIM models, respectively, into point clouds and compared them with the scanned point clouds to achieve automatic structural recognition and progress control. In semantic segmentation, Boyu Wang et al. [33] and Yuandong Pan et al. [34] integrated the rich semantic information of images into point clouds with high geometric accuracy for point cloud segmentation and geometric reconstruction. After the introduction of the deep learning framework PointNet [35] and PointNet++ [36] which directly process point clouds, researchers have explored further applications of this framework, such as building element classification [37,38], concrete surface segmentation [39] and industrial component segmentation [40,41]. Xiaofei Yang et al. [42] used weighted superpoint graph segmentation to achieve automatic semantic segmentation of large-scale point clouds of bridge components. Yang et al. [43] employed a point cloud data augmentation strategy to address the issue of data scarcity by adding synthetic bridge point clouds

to real-world scanning point cloud training sets. However, due to significant deformations during construction, the segmentation of cables may not be sufficient for aligning the entire point cloud model with BIM. Additionally, obtaining substantial data labels, typically required for effective segmentation, may not be always available in real projects. To overcome the limitations of the current object recognition and geometric representations extraction, this study presents an automated geometric modeling method for cable-net structures while simultaneously evaluating cable forces.
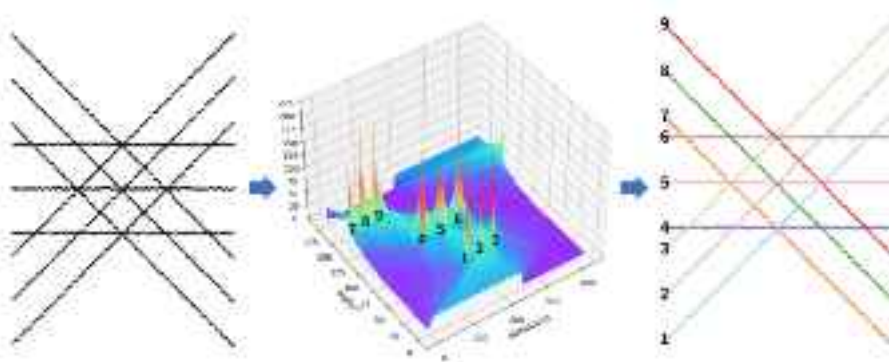
3. Methodology

3.1. Automated segmentation of cable-net point clouds
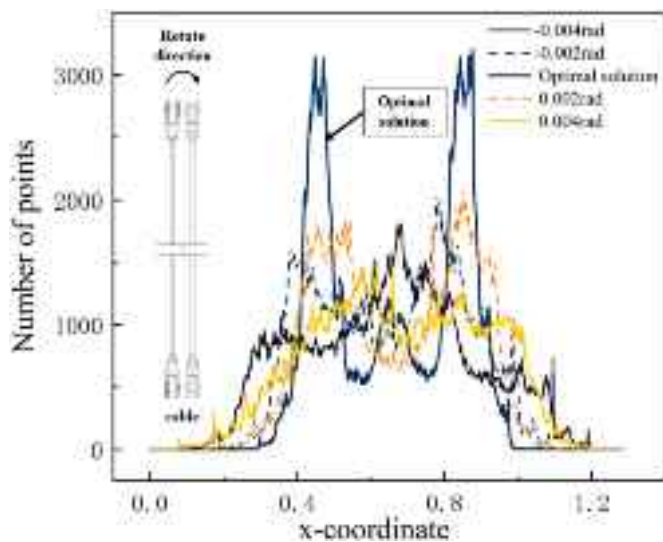
3.1.1. Composition of cables and preliminary extraction of cable point cloud

As shown in Fig. 2, a cable typically consists of three main components, cable clamps, the cable body and the anchorage (including ear plates and anchorage ends). The cable net is first extracted from the point cloud based on the mean curvature. Subsequently, the Hough transform is applied to detect and characterize individual cables. The segmentation of individual cables enables parallel computing, thereby enhancing the efficiency of geometric computations. Each cable is then rotated to align with the global coordinate system for further geometric processing. By default, the cable axis is aligned parallel to the Y-axis after rotation, and all point cloud slices are projected onto the X-Z plane.

In the scanned point cloud of the cable-net structure, the majority of points originate from planar surfaces with zero mean curvatures, while points with positive mean curvatures primarily belong to the cables, such that they can be straightforwardly distinguished from other structural components. The point cloud of a cable body can be approximated as a cylindrical surface, with principal curvatures present in the axis direction of the cable and tangentially perpendicular to it. Ideally, the mean curvatures of points on the cable surface are expected to be $1/2R$ with R denoting the cable radius. Nonetheless, solely relying on mean curvature as a filtering condition for extracting all the cable points can be challenging, due to geometric inaccuracies stemming from factors such as the small sizes of the cables and the considerable scanning distance from the ground. Moreover, interference from other cylindrical members at the construction site, such as scaffolding, may further

**Fig. 3.** Segmentation of individual cable point clouds with Hough transform.

Fig. 4. Point cloud counting along X-axis.
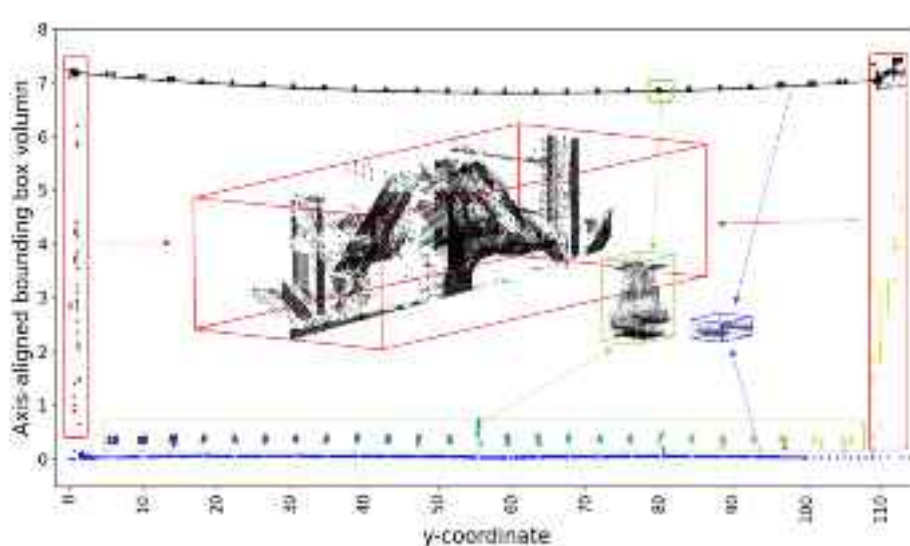
complicate the identification of the cable points.

3.1.2. Segmentation of individual cables
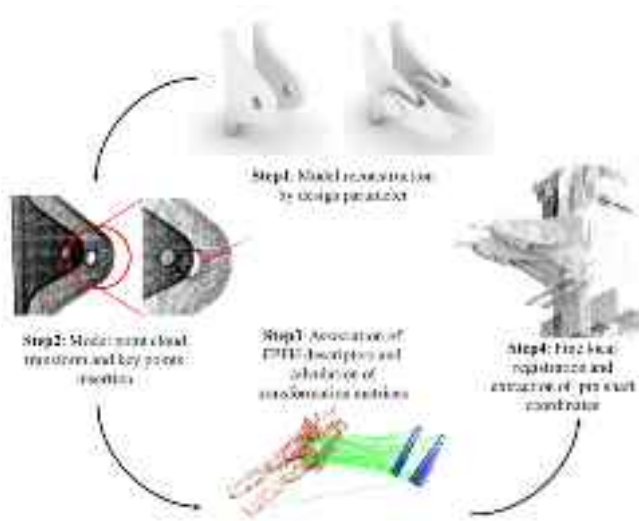
After separating the cable points from the scanned point cloud, the segmentation of individual cables is required. The cable points are first projected onto the X-Y plane, where the projected points are approximated as straight lines. Each line can be parameterized by ρ and θ, with ρ the distance from the origin to the line and θ the perpendicular direction from the origin to the line. A point in the X-Y plane can be represented with a trigonometric curve $\rho = x_1 cos\theta + y_1 sin\theta$. The Hough transform [44] is then applied to compute the parameters ρ and θ of lines in the 2D space. The ρ-θ space is discretized into small girds, and the corresponding curve representation at each grid point is computed. When the curve representation of a point passes through a grid, a vote is cast to the grid. After looping over all the grid points, the grids with the highest votes are considered as candidate lines.

The line equations obtained from the Hough transform can be used to partition the point cloud based on the distance from each line within a specified range, such that the points associated each cable can be determined. As shown in Fig. 3, point clouds of nine cables are manually generated, with noisy points added around each cables within a range of 0.5 m to challenge the Hough transform process. Consequently, each cable has been correctly segmented. However, it should be noted that the presence of noisy points may lead to the identification of multiple lines within a cluster of cable points. To address this issue, candidate lines within a user-defined range of voting scores and non-maximum suppression need to be merged after the Hough voting process. Adjusting the voting scores helps to filter out erroneous candidate lines caused by noise, while the non-maximum suppression range needs fine-tuning to merge the candidates identified as two clusters on a single cable.


Fig. 5. Different regions with AABB (Axis-Aligned Bounding Box) and clustering results.

Fig. 6. Overall workflow of accurate extraction of cable anchorage coordinate.

3.1.3. Coordinate transformation of cable points

The coordinates of cable points need to be transformed into a unified coordinate system to facilitate consistent geometry processing. To this end, the principal direction of the points belonging to each cable is first determined using the principal component analysis (PCA). Subsequently, the points are rotated to align with the global Y-axis. However, the axis alignment after rotation may not be optimal in some cases, as external points can influence the computation of the principal direction. To address this issue, additional small rotations are performed in both clockwise and counterclockwise directions on the cable points. We utilize statistical analysis along the global X-axis to mitigate the influence of the external points on the transformation of cable points. Specifically, the statistical mean square deviation (MSD) is used to determine the optimal rotation direction. In our study the direction with the maximum MSD is considered as the principal direction for rotation, ensuring to transform the cable points to the global coordinate system. Fig. 4 illustrates the rotation of cable points with a small angle and the statistical analysis along the X-axis.

3.2. Automated extraction of crucial points of cables

As illustrated in Fig. 2, the crucial points of a cable include concentrated loading points (e.g. cable clamps), points along the cable axis and pin positions at the anchorage. Distinct strategies are required for the automated extraction of these crucial points.

3.2.1. Extraction of concentrated loading points

In practice, it only needs to compute the coordinates of the concentrated loading points in the Y-axis direction, so that the midpoints of the cable clamps are considered. Firstly, the cable is sliced along the axis direction (Y-axis), and the AABB (axis-aligned bounding box) volume of each slice is computed. In this study, a slice thickness of 5 mm is used. The slice thickness determines the resolution of each slice coordinate, which will affect the calculation accuracy of clamp positions. Fig. 5 demonstrates distinct AABB volumes in the anchorage, cable and cable clamp regions. Hence, it is feasible to extract points in different regions based on the AABB volumes.

Subsequently, the DBSCAN clustering algorithm [45] is applied to the filtered point cloud with the cable clamp region along the Y-axis direction (as depicted by different colors in Fig. 5). Considering the mean of the Y-axis coordinates of each cluster in the point cloud, the positions of concentrated loading points on the cable can be derived. Ultimately, the locations of all concentrated loadings on a single cable

are determined.

3.2.2. Extraction of pin positions at the anchorage

Unlike cable clamps, the position of the pin shaft is not at the middle of the anchorage. To accurately extract the coordinates of the pin shaft, both the elevation coordinate (z-coordinate) and the y-coordinate of the pin shaft are required. Since the position of the pin shaft remains fixed relative to the ear plate in the anchorage region, a model-based registration method is employed for automatic extraction of the coordinates of the pin shaft, as illustrated in Fig. 6.

3.2.2.1. Refinement of anchorage model reconstruction.
During the construction phase, only the ear plate model is generated, as depicted on the left in Step 1 of Fig. 6. However, as the angle between the ear plate and the anchorage end may change under loads applied to the cable, it becomes impractical to adjust the angle between the two models for each registration. Therefore, in the operation and maintenance phase when the relative position between the ear plate and the anchorage end remains fixed, both models are registered, as illustrated on the right in Step 1 of Fig. 6. Additional features are progressively incorporated into the models during subsequent registrations. Following the CAD model reconstruction, the center of the pin shaft is relocated to the origin (0,0,0) to facilitate the subsequent extraction processes.

The construction of the model can be executed in advance based on CAD drawings using commercial software such as Rhino and C4D. The resulting model can be exported in ".stl" format, and point cloud data can be extracted using the Sample Points function. It should be noted that both the modeling process and reference point cloud extraction can be included in the data preparation phase prior to the construction phase.

3.2.2.2. Association of the reference and the scanned point clouds.
For the initial coarse registration between the reference point cloud and the scanned point cloud, the fast feature point histograms (FPFH) descriptors [28] are adopted. These descriptors encodes local features of the point cloud based on the spatial relationship between the feature points and their neighborhood, considering three relevant angular relations. The feature sets are then placed in histograms for vote counting. To ensure accurate association of the two point clouds, both point cloud models are initially downsampled to the same distance before obtaining the feature descriptors. However, applying the existing association and coarse registration algorithms only often fails to produce satisfactory results for small-scale point cloud models due to the possible occlusions and noise present in the scanned point cloud. This is evident in Step 3 of Fig. 6, where not all points in the reference point cloud are correctly associated with those in the scanned point cloud of the ear plates.

As a matter of fact, the registration of the reference and the scanned point clouds of the ear plates can be achieved through translation alone, if the cable points have already been properly rotated to the global coordinate system. The slight angle variations in the ear plates resulting from on-site construction factors can be addressed with the iterative closest point [46] (ICP) algorithm in the preceding rotation and fitting processes. The translation parameters are computed based on the coordinate differences between the associated points in the two point clouds, which form the translation matrix for fine registration using the ICP algorithm, as illustrated in Step 4 of Fig. 6.

3.2.2.3. Extraction of pin shaft coordinates.
Having translated the center of the pin shaft to the origin (0, 0, 0), the origin can now be added to the first index position of the reference point cloud to represent the pin shaft position. Subsequently, the translation matrices derived from the preceding section are used in the ICP algorithm, and the registration errors are computed. Within the loop of ICP operations, the fitness value serves as a filtering criterion. In each ICP registration, the fitness value and the translation matrix are updated if the new fitness value exceeds the
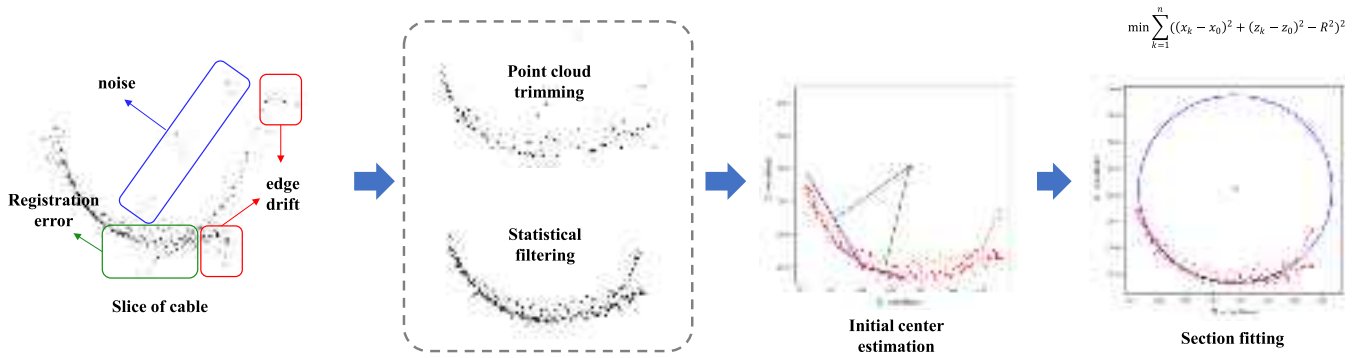
Fig. 7. Fitting of circular cross-sections of cables.

previous one. Upon termination of the iterations, the best registration sets of point cloud models are obtained. The coordinates of the pin shaft after translation and rotation can then be found at the first index position. The registration result is illustrated in Step 4 of Fig. 6. This process is outlined in the following pseudocode.

---

1. Input. Set the reference point cloud and scanned point cloud as *source_point* and *target_point*. Set all the points with the similar feature descriptors in reference model P_r and scanned model P_s as input.

   2. Initialize. *FITNESS* = 0, **T** = [0, 0, 0].

   3. Iterate. Find the best registration between two models.

      FOR i = 1 TO n, n is the number of P_r and P_s.

      3.1 Calculate the initial transformation. $T_i = P_{r,i} - P_{s,i}$

      3.2 ICP Algorithm. icp_result = ICP(*source_point*, *target_point*, T_i)

         IF icp_result.*fitness* > *FITNESS*

            THEN *FITNESS* = icp_result.*fitness*

            T = icp_result.**rotation** * T_i + icp_result.**transformation**

   4. Return **T**

3.2.3. Fitting of the cable cross-section

The fitting of cable cross-sections presents challenges due to their small sizes and issues such as edge drift and registration errors during scanning. Consequently, the fitted radius of the cable cross-section may exhibit inconsistency, directly affecting the accuracy of the axis point coordinates. In construction scenarios, the dimensions of cable cross-sections are generally consistent, with manufacturing errors typically within sub-millimeter ranges. Therefore, there is generally no need to use point cloud scanning to correct the dimensions of cable cross-sections. Instead, we recommend employing circle templates to fit the coordinates of axial points.

As illustrated in Fig. 7, it is essential to "trim" the surrounding points of the cross-section prior to fitting, in order to eliminate potential edge drift resulting from scanning cylindrical or spherical objects. We propose trimming off approximately 10% of the points. Additionally, statistical filtering is applied to eliminate the noise generated in the scanning process. After trimming the point cloud, only a half or quarter of a circle of points may remain, which is adequate for fitting a circle with a known radius. Fitting a circular cross-section can be described as solving a nonlinear optimization problem, i.e.,

$$min\sum_{k=1}^{n}\left((x_k - x_0)^2 + (z_k - z_0)^2 - R^2\right)^2 \tag{1}$$

To provide a good initial guess of the circle center, the points are first sorted by their Z-axis coordinates, and the coordinates of the highest, lowest and middle points are selected. The intersection point of the perpendicular bisectors of any two selected points is considered as the initial guess for the nonlinear optimization.

3.3. Extraction of cable shapes and cable forces

The cable shape under the self-weight loading can be accurately
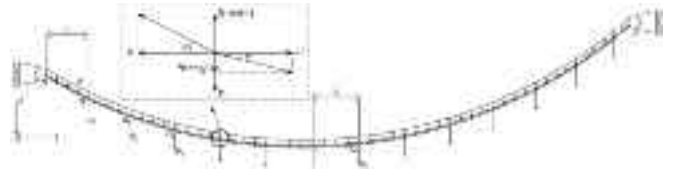
Fig. 8. Force diagram of a cable.

represented by a catenary curve. Instead of commonly employed methods for obtaining the shape of the steel structure, cable shapes and cable forces can be determined with the nonlinear iterative method based on the segmented catenary theory. This method proves more efficient compared with the traditional approaches that rely on fitting the axis line with numerous slices. Besides, it is suitable for cases where the cable point cloud is incomplete or of poor quality. The segmented catenary theory computes the final geometric configuration of a cable, considering factors such as initial cable length, pre-tension and temperature effects, if the change in cross-sectional area of the cable before and after deformation is not considered.

As shown in Fig. 8, in the segmented catenary theory [47], each segment of the catenary curve is expressed as

$$f_i(y) = c\left[cosh\left(\frac{y}{c} + a_i\right) - cosh\, a_i\right] \tag{2}$$

$$c = -\frac{H}{q} \tag{3}$$

where i is the segment index of the curve, H is the horizontal force in the cable, q is the linear self-weight of the cable, and a_i are the parameters of the catenary curve. The equilibrium at the location of a concentrated load is computed as

$$H \cdot tan\,\alpha = H \cdot tan\beta + P_i \tag{4}$$

$$tan\alpha = (f_i(l_i))' = sinh\left(\frac{l_i}{c} + a_i\right) \tag{5}$$

$$tan\beta = (f_{i+1}(0))' = sinh(a_{i+1}) \tag{6}$$

Combining eqs. (4), (5) and (6) yields

$$H \cdot sinh\left(\frac{l_i}{c} + a_i\right) = H \cdot sinh(a_{i+1}) + P_i \tag{7}$$

where l_i is the distance between each segment, obtained from computing the coordinates of cable anchorage points and the y-coordinates of the cable clamps through the point cloud scanning. P_i is the magnitude of the concentrated load which is the sum of the weights of the connecting member and the cable clamp. Based on eq. (7), all the parameters a_i can be represented by a_1 through the recursive method.
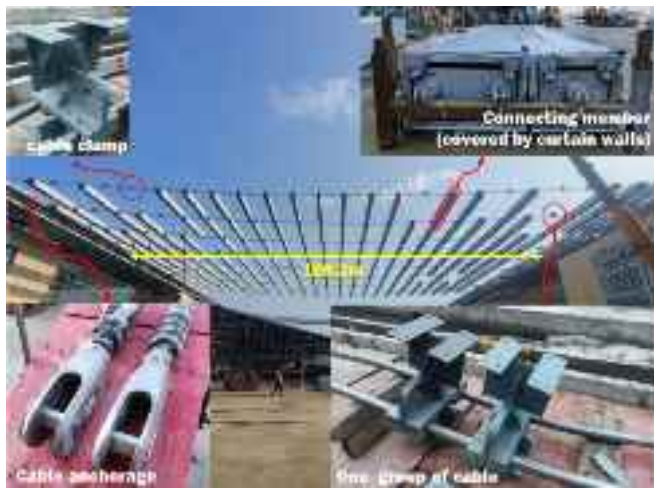
Fig. 9. On-site view of the cable-net structure.

Fig. 10. Cables are tensioned by hydraulic jacks on site.

Table 1
Diameters of the cable cross-sections.

Cable number	Position1/ mm	Position2/ mm	Position 3/ mm	Average/ mm
13–1	71.18	71.12	71.16	71.15
13–2	71.18	71.26	71.10	71.18
14–1	71.14	71.16	71.18	71.16
14–2	71.18	71.24	71.16	71.19

Table 2
Design parameters of the cables.

Parameter	Value
Material	1.4401 (X5CrNiMo17–12-2)
Weight per Meter	Approximately 26 kg/m
Metal Cross Section Area	3128 mm^2
Minimum Breaking Load	4169 kN
Ultimate Working Load	2779 kN
Young's Modulus	130 ± 10 kN/mm^2
Thermal Expansion Coefficient	16 × 10^{-6}/°C
Creep Coefficient	Approximately 0.015%

Based on the methodology proposed in [47] for determining the configuration of cables, we have the following constraint conditions for the y-coordinates of concentrated loads,

$$g' = c \sum_{i=1}^{m} \left[cosh\left(\frac{y}{c} + a_i\right) - cosh a_i \right] - \Delta oo' \tag{8}$$

$$g_1 = c \sum_{i=1}^{1} \left[cosh\left(\frac{y}{c} + a_i\right) - cosh a_i \right] - \Delta oo_1 \tag{9}$$

$$g_2 = c \sum_{i=1}^{2} \left[cosh\left(\frac{y}{c} + a_i\right) - cosh a_i \right] - \Delta oo_2 \tag{10}$$

$$\ldots$$

$$g_n = c \sum_{i=1}^{n} \left[cosh\left(\frac{y}{c} + a_i\right) - cosh a_i \right] - \Delta oo_n \tag{11}$$

where m is the total number of segment curves between oo', and n is the number of the segment curves between oo_n, g' measures the deviation between the accumulation of elevation differences of all calculated segment curves and $\Delta oo'$ in the Z-direction, Δoo_i is the sag of the cable at different concentrated load positions, which is given by

$$\Delta oo_i = z_o - z_{o_i} \tag{12}$$

By minimizing the following nonlinear equation

$$F = g'^2 + g_i^2 + \ldots \tag{13}$$

the values of c and a_i can be obtained, followed by the computation of the cable shape and the tension H. It is important to note that at least two control equations, g' and g_i ($i > 0$), are required to accurately describe the cable shape. It is recommended to select the locations with high-quality point cloud scanning and significant sag for g_i. As the number of control equations increases, the obtained cable shape becomes closer to the true shape, resulting in more accurate tension forces.

4. Experiments and validation

4.1. Project overview

The proposed approach has been validated with a single-curve cable-net structure in the construction phase. The structure spans 109.2 m in the north-south direction and 160 m in the east-west direction. It consists of 18 groups of cables spanning in the north-south direction, with each group composed of two cables. Circular tubes are used to connect two groups of cables through cable clamps. The connecting members wrapped with curtain walls are employed for the lifting and installation of the cables. Fig. 9 is the panoramic view of the project. Fig. 10 illustrate the tensioning of cables using hydraulic jacks on site. The construction scheme involves several stages. Initially, the cable clamps are installed at specified locations on the cables (see the cable diagram in Table 4). Subsequently, the cables are tensioned to achieve the optimal performance. Once the adjacent groups of cables are successfully tensioned and secured, connecting members are installed between them. To streamline identification, the cables are systematically labeled from west to east as #1 to #18, while the connecting members are sequenced from south to north as #1 to #25. For computational simplicity, groups of cables are simplified as single cables with doubled cross-sectional areas.

4.2. Parameters setting

4.2.1. Design parameters

The cross-sectional dimensions of the two groups of cables (4 cables in total) were measured using a vernier caliper with an accuracy of 0.02 mm. Measurements were taken at three different positions on each of the four cables, and the measured diameters are recorded in Table 1. It can be observed that the variances of the measured diameters of the four cables are all within 0.05 mm. Therefore, a standardized cross-section radius of 35.6 mm will be employed uniformly in the subsequent cross-section fitting procedure. Additional parameters of the cables can
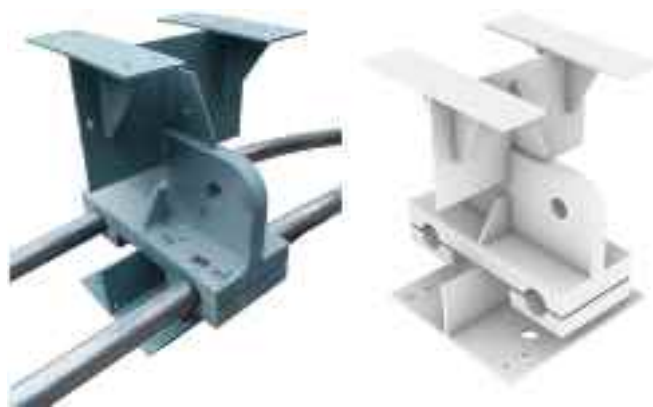
Fig. 11. On-Site Image and Modeling Diagram of cable clamp.

Table 3
Design parameters of connecting members.

Position	Width/ mm	Height/ mm	Length/ mm	Weight/ kg
#1 / #25	1500.00	1000.00	7550.00	2157.32
#2 / #24	1300.00	1000.00	7550.00	2089.09
#3 / #23	1200.00	1000.00	7550.00	2054.98
#4 / #22	1100.00	1000.00	7550.00	1540.49
#5 / #21	1000.00	1000.00	7550.00	1506.38
#6 / #20	900.00	1000.00	7550.00	1472.27
#7 / #19	800.00	1000.00	7550.00	1431.37
#8 / #18	750.00	1000.00	7550.00	1414.31
#9 / #17	700.00	1000.00	7550.00	1397.26
#10 / #11 / #15 / #16	650.00	1000.00	7550.00	1380.20
#12 / #13 / #14	600.00	1000.00	7550.00	1363.14

be found in Table 2.

The cable clamps were modeled in Rhino, as shown in Fig. 11. The estimated volume of the cable clamp, calculated using Rhino, is 24,149,967.8 mm^3. With the density of the steel material assumed as 7850 kg/m^3, the cable clamp is estimated to weigh 189.58 kg. The weights of connecting members are provided in Table 3.

4.2.2. Scanning parameters

The 3D laser scanner deployed in the project is the Leica ScanStation P40, with a scanning accuracy of 1.2 mm + 10 ppm. The scan data is processed with a multi-station registration technique, combining the target-based and the manual registration methods. The point cloud resolution for each scanning station is 3.1 mm @ 10 m. For the case discussed in Section 4.4, the complete scanning results are displayed in Fig. 12. Six scanning stations (Scan1 – Scan6) were utilized throughout the scanning process, with seven targets (t1-t7) employed for point cloud registration. The location of the laser scanner and targets are shown in Fig. 12.

4.3. Validation of cable shapes and forces

In this study, we focus on the initial cable shapes, which are formed by tensioning the cables with the hydraulic pressure after installing the cable clamps. During the on-site scanning, no connecting members are installed on the cables, and the only concentrated loads are the weights of the cable clamps. To verify the theoretical computation of the cable force, we use the final cable tension measured by the hydraulic pressure gauge during the initial tensioning process. The accuracy of theoretical cable shapes is validated by comparing them with the fitted cable shapes derived from the point cloud. During the multiple scans in the construction phase, a total of eight groups of initial cable shapes were extracted. The segment spacing measured through point cloud between the clamps are recorded in Table 4.

The specific process for extracting the cable forces and shapes is illustrated in Fig. 13. Initially, crucial points are extracted from each
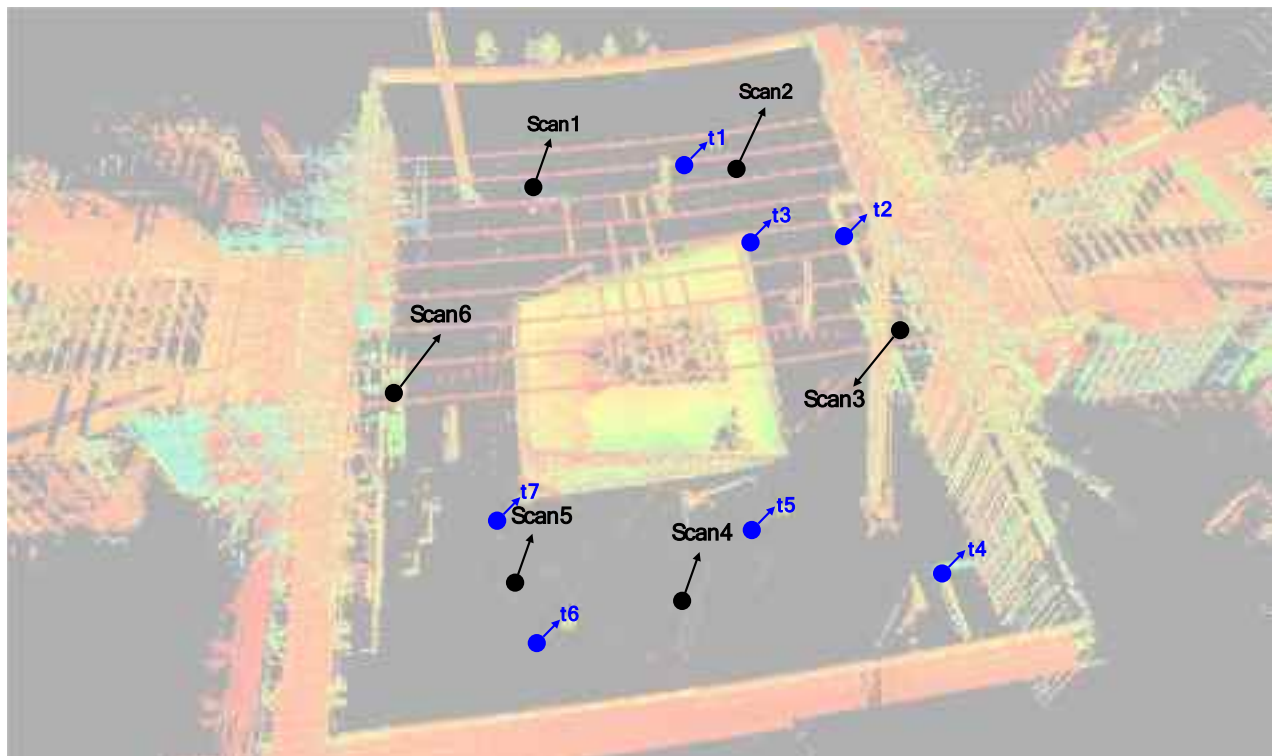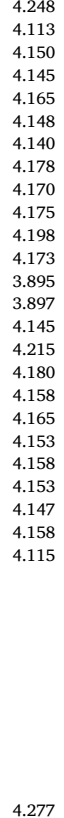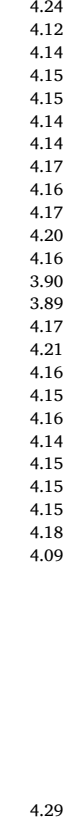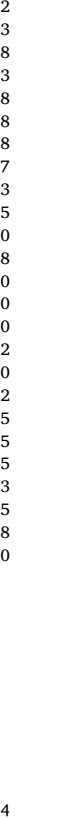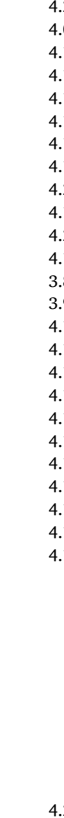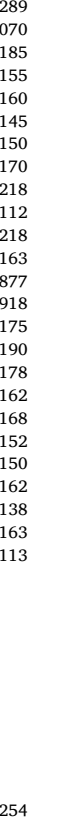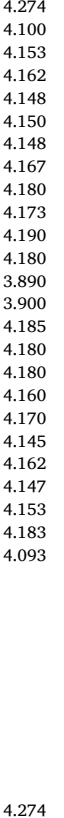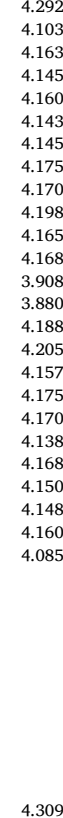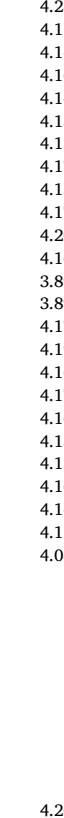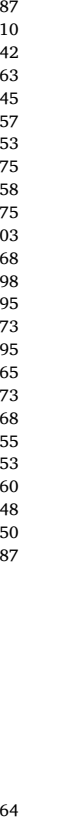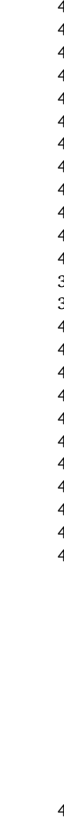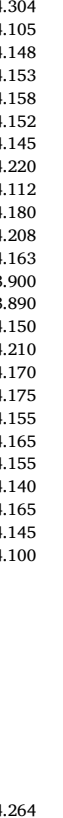

Fig. 12. Scanning results and position of scans and targets.

Table 4
Segment spacing.

| Cable diagram	cable1 /m	cable2 /m	cable3 /m	cable4 /m	cable5 /m	cable7 /m	cable13 /m	cable14 /m
	4.248	4.242	4.289	4.274	4.292	4.287	4.304	4.279
	4.113	4.123	4.070	4.100	4.103	4.110	4.105	4.080
	4.150	4.148	4.185	4.153	4.163	4.142	4.148	4.173
	4.145	4.153	4.155	4.162	4.145	4.163	4.153	4.160
	4.165	4.158	4.160	4.148	4.160	4.145	4.158	4.140
	4.148	4.148	4.145	4.150	4.143	4.157	4.152	4.145
	4.140	4.148	4.150	4.148	4.145	4.153	4.145	4.155
	4.178	4.177	4.170	4.167	4.175	4.175	4.220	4.180
	4.170	4.163	4.218	4.180	4.170	4.158	4.112	4.172
	4.175	4.175	4.112	4.173	4.198	4.175	4.180	4.165
	4.198	4.200	4.218	4.190	4.165	4.203	4.208	4.203
	4.173	4.168	4.163	4.180	4.168	4.168	4.163	4.150
	3.895	3.900	3.877	3.890	3.908	3.898	3.900	3.905
	3.897	3.890	3.918	3.900	3.880	3.895	3.890	3.898
	4.145	4.170	4.175	4.185	4.188	4.173	4.150	4.172
	4.215	4.212	4.190	4.180	4.205	4.195	4.210	4.178
	4.180	4.160	4.178	4.180	4.157	4.165	4.170	4.185
	4.158	4.152	4.162	4.160	4.175	4.173	4.175	4.173
	4.165	4.165	4.168	4.170	4.170	4.168	4.155	4.173
	4.153	4.145	4.152	4.145	4.138	4.155	4.165	4.153
	4.158	4.155	4.150	4.162	4.168	4.153	4.155	4.143
	4.153	4.153	4.162	4.147	4.150	4.160	4.140	4.157
	4.147	4.155	4.138	4.153	4.148	4.148	4.165	4.158
	4.158	4.188	4.163	4.183	4.160	4.150	4.145	4.143
	4.115	4.090	4.113	4.093	4.085	4.087	4.100	4.105
	4.277	4.294	4.254	4.274	4.309	4.264	4.264	4.303
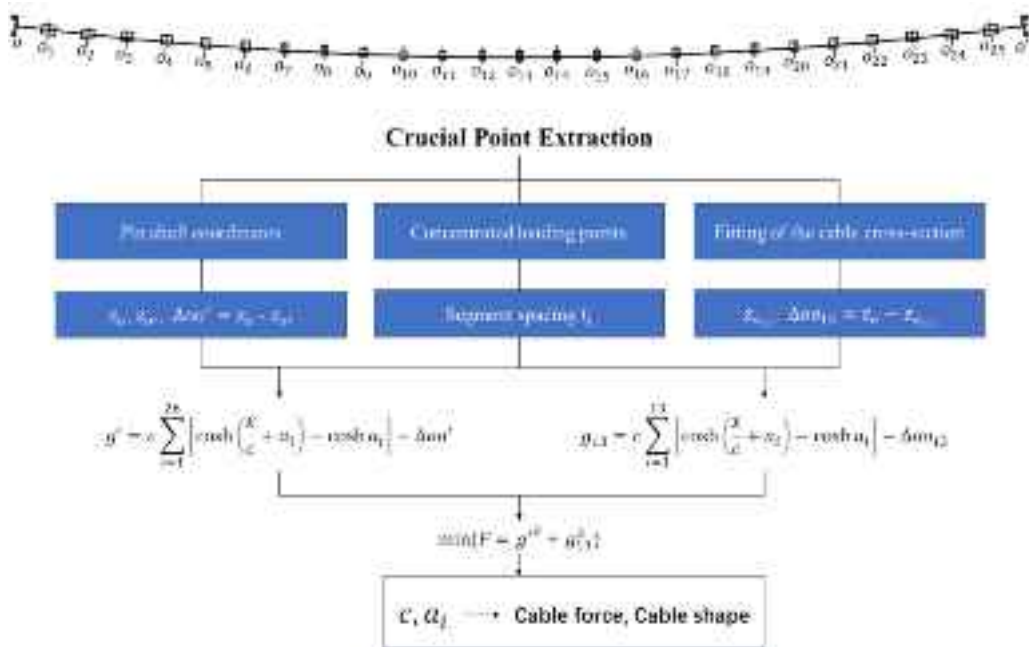
Fig. 13. Calculated force over cable length.

Table 5
Comparison of calculated and measured cable forces.

No.	Height of anchorage1 (m)	Height of anchorage2 (m)	Height of middle (m)	Sag1 (m)	Sag2 (m)	Calculated force (kN)	Pressure gauge (kN)	Error
1	27.561	27.537	25.463	0.024	2.098	690.1579	666.6	3.534%
2	27.552	27.532	25.548	0.020	2.004	722.0067	690.8	4.517%
3	27.536	27.548	25.522	−0.012	2.015	712.5960	723.4	−1.494%
4	27.413	27.394	25.229	0.019	2.184	662.2879	639.6	3.547%
5	27.409	27.374	25.223	0.035	2.186	664.4604	666.8	−0.351%
7	27.387	27.363	25.185	0.024	2.202	657.8351	659.765	−0.293%
13	27.412	27.439	25.212	−0.027	2.201	650.7119	668.4	−2.646%
14	27.433	27.405	25.225	0.028	2.208	656.6366	643.1	2.105%

Table 6
Robustness of cable force inference.

No.	Correct height/m	Height error/mm	Calculated height/m	Calculated force/kN	error
13#	−2.098	0	−2.098	690.158	0.000%
13#	−2.098	10	−2.088	693.481	0.481%
13#	−2.098	−10	−2.108	686.866	−0.477%
10#	−1.989	0	−1.989	690.081	−0.011%
10#	−1.989	10	−1.979	693.583	0.496%
10#	−1.989	−10	−1.999	686.616	−0.513%
8#	−1.812	0	−1.812	683.944	−0.900%
8#	−1.812	10	−1.802	687.744	−0.350%
8#	−1.812	−10	−1.822	680.17	−1.447%

cable to determine parameters such as sags and segment spacing. Subsequently, two control equations g_0 and g_{13} are selected. Through iterative computation of the minimum value of F, the parameters c and a_i can be obtained. Following this, the cable shape and the tension H can be computed accordingly.

4.3.1. Validation of cable forces

The cable forces for each cable group, comprising the sum of two cables, are inferred with the method described and compared against the final cable tensions recorded by the hydraulic pressure gauge. Table 5 presents the comparison results, where Sag1($\Delta oo'$) is the height difference between anchorage1 and anchorage2, and Sag2(Δoo_{13}) is the height difference between anchorage1 and the middle of the cable. It is evident from Table 5 that the errors of the calculated cable forces are within 5%, which demonstrates the accuracy of the proposed calculation method.

The cable forces in Table 5 account for the mid-span sag at the #13 cable clamp position. To demonstrate the robustness of the method, the sag heights at the #8, #10 and #13 cable clamp positions were used as constraint conditions to compute the force of cable 1. These results, presented in Table 6, were calculated following the procedure outlined in Fig. 13, with adjustments made to replace the formula g_{13} with g_{10} and g_8. Furthermore, the values of Δoo_{13}, Δoo_{10} and Δoo_8 were adjusted by ±10 mm for calculation, and the calculated cable forces were compared with the original values to assess the influence of measurement errors on cable sags. The results reveal that the measured errors are within 10 mm, with variations in the inferred cable forces of <1%. Moreover, the computation of the cable forces considering different elevations of the concentrated loading positions demonstrates robustness, with errors remaining under 1%. Additionally, a scanning accuracy of 1.2 mm + 10 ppm is sufficient for meeting the needs of cable force extraction.

4.3.2. Validation of cable shapes

For ease of visualization, we only present a comparison between three tensioned cables #1, #2 and #13, focusing on their shapes obtained from the proposed method and those fitted from slices. As shown in Fig. 14, the theoretical cable shapes closely align with those obtained

(a) Comparison of cable shapes between fitting curves and theoretical curves

(b) Deviations of cable shapes between fitting curves and theoretical curves
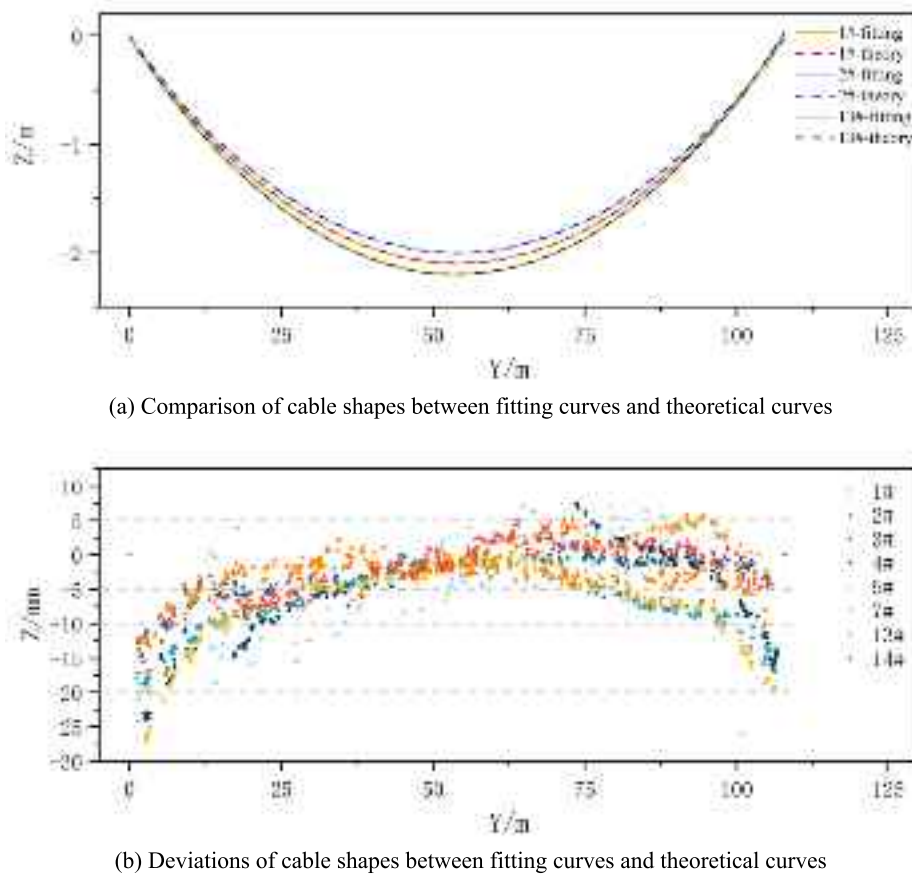
Fig. 14. Comparison of cable shapes and shape deviations.

Table 7
Comparison of calculation efficiency.

Num.	Number of points	Extraction by slicing and fitting/s	Extraction by segment catenary theory/s
1#	1,217,678	2253.02	7.54
2#	735,407	1531.89	7.58
3#	770,042	1248.64	7.51
4#	795,364	1363.17	7.62
5#	536,795	745.29	7.54
7#	614,193	712.96	7.61
13#	552,214	756.66	7.57
14#	548,123	742.77	7.51

from slice fitting. The elevation difference between the slice-fitted cable shapes and the calculated shapes at the same positions is also evaluated. Smaller shape deviations at around 60 m are observed than other locations of cables. In the anchorage, discrepancies of 10 mm to 25 mm exist between the fitted and theoretical cable shapes. Deviations elsewhere remain within ±5 mm. These discrepancies stem from the elevation constraint condition in theoretical calculations that considers the mid-span elevation be consistent with the actual mid-span elevation, as well as the absence of consideration for the self-weight of the cable anchorage in the theoretical calculations. Moreover, during the fitting process, it was found that the horizontal deformation is minimal (around 1/2000), indicating significant horizontal stiffness provided by the connecting members between the cables.

The runtime comparison between the two methods using the same cross-sectional fitting approach is listed in Table 7. It can be observed that the catenary theory based method significantly reduces the time required for extracting cable shapes compared with the slicing method.

Furthermore, it is noteworthy that while the runtime of the slicing method scales with the number of points, the theoretical calculations remain unaffected by the number of points.

4.4. Evaluation of large-scale point cloud processing

The point cloud model scanned at the construction site (Fig. 15) contains nine cables with various connecting members, even after downsampling, retaining 24,014,289 points. All nine cables are subjected to varying concentrated loading. The main steps of the cable net processing procedure are depicted in Fig. 15, and the cable forces are given in Table 8. The processing initiates with the raw point cloud as follows:

(1) Mean curvature calculation and filtering: With the open-source library CloudCompare, the mean curvature of the point cloud is computed, followed by the extraction of cylindrical point clouds through mean curvature filtering.

(2) Hough Transform for cable segmentation: The Hough transform is utilized to identify and segment the cables in the point cloud, as indicated in the workflow diagram by the steps of curvature calculation and Hough transform.

(3) Refinement of cable point clouds: After curvature filtering, certain cable point cloud information may be lost, resulting in fragmented cable point clouds, as shown in Step 2 of the workflow. To address this issue, the line parameters obtained from the Hough transform are reapplied to the raw point cloud, ensuring complete data retrieval for all nine cables.

(4) Coordinate transformation: Coordinate transformations are executed to align the cable directions with the Y-axis for each cable.

(5) Extraction of key coordinates: Key coordinates are extracted from
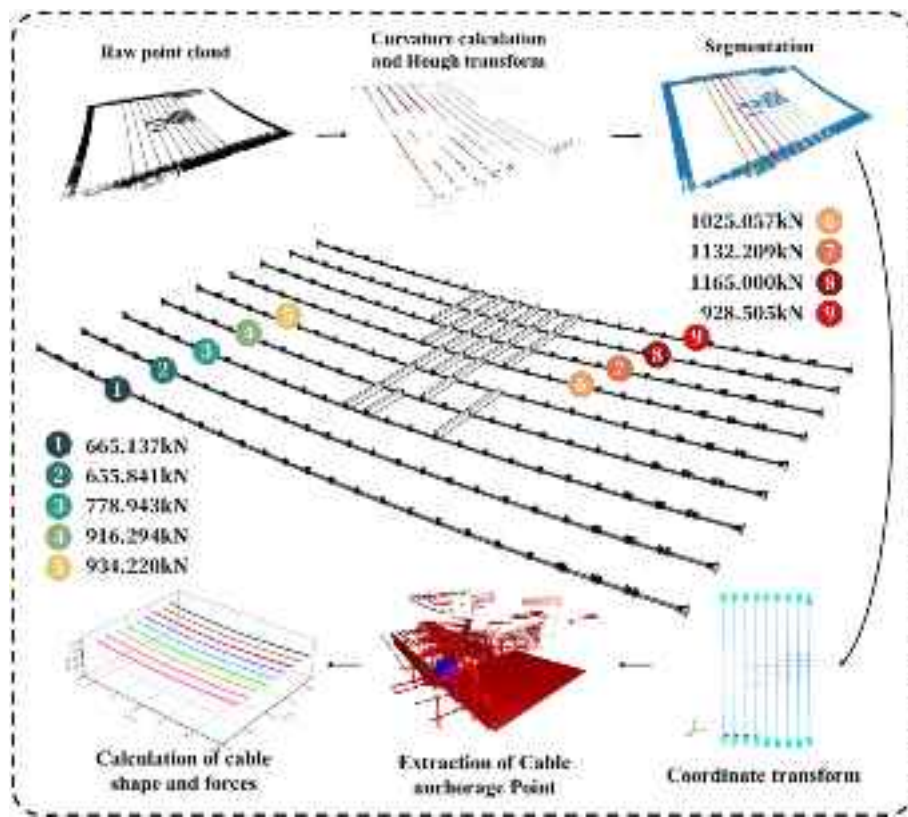
Fig. 15. Cable-net point cloud processing procedure.

Table 8
Cable force results.

Num.	Height of anchorage1/m	Height of anchorage2/m	Height of 10#clamp/m	sag1/m	Sag2/m	calculated force/kN
4	27.410	27.393	25.350	0.017	2.060	665.137
5	27.413	27.378	25.314	0.035	2.099	655.841
6	27.412	27.413	25.145	−0.0006	2.267	778.943
7	27.407	27.386	25.028	0.021	2.379	916.294
8	27.417	27.357	25.091	0.060	2.326	934.220
9	27.331	27.400	25.031	−0.069	2.300	1025.057
10	27.400	27.582	24.997	−0.182	2.403	1132.209
11	27.387	27.396	24.961	−0.009	2.426	1165.000
12	27.387	27.403	25.135	−0.016	2.252	928.505

each cable, as indicated in the workflow diagram, showing the registration results between the anchor plate model and the scanned point cloud for extracting the pin coordinates. The extraction of cable clamp coordinates and cable cross-section coordinates is depicted in Figs. 5 and 7, respectively.

(6) Calculation of cable forces and shapes: The forces and shapes of all nine cables are determined through segmented catenary theory and nonlinear optimization. Subsequently, the cable net is modeled using Rhino software.

Fig. 15 illustrates that with an increase in the number of connecting members, the deflection at the middle of the cable gradually amplifies, alongside an increase in cable forces. It should be noted that the force in cable #8 is higher than cable #9 due to the connecting members installed on both sides of cable #8, while cable #9 only has connecting members on one side, resulting in relatively a smaller cable force.

Throughout the framework, several techniques are applied to mitigate the effects of noise. Mean curvature filtering and Hough votes filtering during segmentation eliminate the non-cylindrical noise and erroneous line extraction due to noise. Additional small rotations are performed for individual cables to minimize the influence of external points on the computation of the principal direction. In the extraction of crucial points, we applied the model-based registration method to match as many points as possible to the model and reduce noise and occlusion effects. Furthermore, trimming surrounding points of the cross-section before fitting helps remove possible edge drift when scanning cylindrical or spherical objects, and statistical filtering is applied to remove the noise generated in the scanning process.

5. Conclusions

This paper presented an automated and precise geometric reconstruction approach for scanned point clouds of cable-net structures, which is a complete workflow from raw point cloud data processing to the extraction of cable shapes and forces. Cables in the raw point cloud are first identified and segmented using a combination of mean curvature filtering and the Hough transform. The cable points are then transformed to the global coordinate system based on principal component analysis and statistical variance. Different components of a

cable, including the anchorage, cable clamps and the cable body, are distinguished using AABB volumes. Cable clamps are extracted using DBSCAN clustering, and the cable cross-sections are fitted with fixed circles. Fast point feature histograms and the iterative closest point algorithm are utilized for the accurate registration between the reference model and the scanned point cloud of the anchorage. Finally, cable forces and shapes are extracted based on the segmented catenary theory.

The proposed method has been validated with a single-curvature cable structure. The accuracy of cable geometry fitting is within ±5 mm and the errors in force extraction are <5%. Additionally, the extraction of cable shapes and forces by fitting a small number of slices and theoretical calculations significantly reduces processing time compared with the method relying on fitting a large number of slices to extract the cable centroids. The proposed method effectively handles the cable-net point cloud with over 20 million points, demonstrating its scalability and efficiency.

Moreover, the proposed method is applicable beyond single-curvature cable-net structures to other cable structures, such as double-curvature cable structures, suspension bridges or cable-stayed bridges. The key step of segmenting point clouds and extracting individual cables in different directions is a general process suitable for various cable structures. Once the point clouds of a structure are segmented into individual cables, the subsequent processing steps remain the same as long as each cable adheres to the catenary assumption. However, there are still some limitations of this method. Challenges in determining the magnitude of concentrated loads applied to individual cables in double-curvature cable structures persist, particularly in distributing the load applied by the self-weight of a cable clamp between two cables. It is usually necessary to introduce both the initial cable tensions and initial concentrated load distributions into iterative calculations, along with additional constraints on cable elevations. Additionally, the effect of the wind-induced vibration of the cables is not considered due to the significantly lower frequency of laser scanning compared to wind-induced vibrations. The static cable forces measured in this study are typically much greater than the cable tension changes caused by wind-induced vibrations. Addressing the effect of wind-induced vibrations would be a focus for future research. The changes in cable tension caused by wind-induced vibrations can be calculated by using accelerometers installed on site and finite element analysis. In the future work, our aim is to convert the obtained models into data structures suitable for numerical analysis and utilize the extracted crucial points for automated BIM (Building Information Modeling) model reconstruction of cable-net structures, further enhancing the efficiency and accuracy of cable-net structure analysis and design process.

CRediT authorship contribution statement

Siwei Lin: Writing – original draft, Visualization, Validation, Methodology, Investigation, Formal analysis, Data curation, Conceptualization. **Liping Duan:** Writing – review & editing, Supervision, Project administration. **Jiming Liu:** Writing – review & editing, Supervision, Investigation. **Xiao Xiao:** Writing – review & editing, Supervision. **Ji Miao:** Writing – review & editing, Investigation. **Jincheng Zhao:** Writing – review & editing, Supervision, Resources, Project administration, Funding acquisition.

Declaration of competing interest

The authors declare that they have no known competing financial interests or personal relationships that could have appeared to influence the work reported in this paper.

Data availability

Data will be made available on request.

References

[1] F. Tao, H. Zhang, A. Liu, A.Y.C. Nee, Digital twin in industry: state-of-the-art, IEEE Trans. Industr. Inform. 15 (2019) 2405–2415, https://doi.org/10.1109/TII.2018.2873186.

[2] V. Pătrăucean, I. Armeni, M. Nahangi, J. Yeung, I. Brilakis, C. Haas, State of research in automatic as-built modelling, Adv. Eng. Inform. 29 (2015) 162–171, https://doi.org/10.1016/j.aei.2015.01.001.

[3] Á. Gómez-Gutiérrez, J. De Sanjosé-Blasco, J. De Matías-Bejarano, F. Berenguer-Sempere, Comparing two photo-reconstruction methods to produce high density point clouds and DEMs in the Corral del Veleta Rock Glacier (Sierra Nevada, Spain), Remote Sens. 6 (2014) 5407–5427, https://doi.org/10.3390/rs6065407.

[4] Y. Xu, J. Zhang, UAV-based bridge geometric shape measurement using automatic bridge component detection and distributed multi-view reconstruction, Autom. Constr. 140 (2022) 104376, https://doi.org/10.1016/j.autcon.2022.104376.

[5] F. He, T. Zhou, W. Xiong, S. Hasheminnasab, A. Habib, Automated aerial triangulation for UAV-based mapping, Remote Sens. 10 (2018) 1952, https://doi.org/10.3390/rs10121952.

[6] Y. Han, D. Feng, W. Wu, X. Yu, G. Wu, J. Liu, Geometric shape measurement and its application in bridge construction based on UAV and terrestrial laser scanner, Autom. Constr. 151 (2023) 104880, https://doi.org/10.1016/j.autcon.2023.104880.

[7] C. Achille, A. Adami, S. Chiarini, S. Cremonesi, F. Fassi, L. Fregonese, L. Taffurelli, UAV-based photogrammetry and integrated technologies for architectural applications—methodological strategies for the after-quake survey of vertical structures in Mantua (Italy), Sensors 15 (2015) 15520–15539, https://doi.org/10.3390/s150715520.

[8] F. Bosché, M. Ahmed, Y. Turkan, C.T. Haas, R. Haas, The value of integrating Scan-to-BIM and Scan-vs-BIM techniques for construction monitoring using laser scanning and BIM: the case of cylindrical MEP components, Autom. Constr. 49 (2015) 201–213, https://doi.org/10.1016/j.autcon.2014.05.014.

[9] Y. Zhou, Z. Xiang, X. Zhang, Y. Wang, D. Han, C. Ying, Mechanical state inversion method for structural performance evaluation of existing suspension bridges using 3D laser scanning, Comput. Aided Civ. Inf. Eng. 37 (2022) 650–665, https://doi.org/10.1111/mice.12765.

[10] Z. Zhang, G. Shi, L. Hou, L. Zhou, Geometric dimension and imperfection measurements of box-T section columns using 3D scanning, J. Constr. Steel Res. 183 (2021) 106742, https://doi.org/10.1016/j.jcsr.2021.106742.

[11] D.F. Laefer, L. Truong-Hong, Toward automatic generation of 3D steel structures for building information modelling, Autom. Constr. 74 (2017) 66–77, https://doi.org/10.1016/j.autcon.2016.11.011.

[12] A. Smith, R. Sarlo, Automated extraction of structural beam lines and connections from point clouds of steel buildings, Comput. Aided Civ. Inf. Eng. 37 (2022) 110–125, https://doi.org/10.1111/mice.12699.

[13] P. Feng, Y. Zou, L. Hu, T. Liu, Use of 3D laser scanning on evaluating reduction of initial geometric imperfection of steel column with pre-stressed CFRP, Eng. Struct. 198 (2019) 109527, https://doi.org/10.1016/j.engstruct.2019.109527.

[14] R. Chacón, C. Puig-Polo, E. Real, TLS measurements of initial imperfections of steel frames for structural analysis within BIM-enabled platforms, Autom. Constr. 125 (2021) 103618, https://doi.org/10.1016/j.autcon.2021.103618.

[15] Y. Xu, M. Zhang, S. Yang, B. Zheng, Measurement and qualification of welded I-column failure mode using laser scanning technique, Structures 34 (2021) 2694–2707, https://doi.org/10.1016/j.istruc.2021.09.040.

[16] Z. Xu, Y. Liang, Y. Xu, Z. Fang, U. Stilla, Geometric modeling and surface-quality inspection of prefabricated concrete components using sliced point clouds, J. Constr. Eng. Manag. 148 (2022) 04022087, https://doi.org/10.1061/(ASCE)CO.1943-7862.0002345.

[17] X. Zhao, M. Tootkaboni, B.W. Schafer, Laser-based cross-section measurement of cold-formed steel members: model reconstruction and application, Thin-Walled Struct. 120 (2017) 70–80, https://doi.org/10.1016/j.tws.2017.08.016.

[18] L. Yang, J.C.P. Cheng, Q. Wang, Semi-automated generation of parametric BIM for steel structures based on terrestrial laser scanning data, Autom. Constr. 112 (2020) 103037, https://doi.org/10.1016/j.autcon.2019.103037.

[19] Y. Yan, J.F. Hajjar, Geometric models from laser scanning data for superstructure components of steel girder bridges, Autom. Constr. 142 (2022) 104484, https://doi.org/10.1016/j.autcon.2022.104484.

[20] J. Lee, H. Son, C. Kim, C. Kim, Skeleton-based 3D reconstruction of as-built pipelines from laser-scan data, Autom. Constr. 35 (2013) 199–207, https://doi.org/10.1016/j.autcon.2013.05.009.

[21] Q. Wu, K. Xu, J. Wang, Constructing 3D CSG models from 3D raw point clouds, Computer Graphics Forum 37 (2018) 221–232, https://doi.org/10.1111/cgf.13504.

[22] T.J.R. Hughes, J.A. Cottrell, Y. Bazilevs, Isogeometric analysis: CAD, finite elements, NURBS, exact geometry and mesh refinement, Comput. Methods Appl. Mech. Eng. 194 (2005) 4135–4195, https://doi.org/10.1016/j.cma.2004.10.008.

[23] A. Dimitrov, R. Gu, M. Golparvar-Fard, Non-uniform B-spline surface fitting from unordered 3D point clouds for as-built modeling, Comput. Aided Civ. Inf. Eng. 31 (2016) 483–498, https://doi.org/10.1111/mice.12192.

[24] A. Ursini, A. Grazzini, F. Matrone, M. Zerbinatti, From scan-to-BIM to a structural finite elements model of built heritage for dynamic simulation, Autom. Constr. 142 (2022) 104518, https://doi.org/10.1016/j.autcon.2022.104518.

[25] C. Rausch, C. Haas, Automated shape and pose updating of building information model elements from 3D point clouds, Autom. Constr. 124 (2021) 103561, https://doi.org/10.1016/j.autcon.2021.103561.

[26] S. Pu, G. Vosselman, Knowledge based reconstruction of building models from terrestrial laser scanning data, ISPRS J. Photogramm. Remote Sens. 64 (2009) 575–584, https://doi.org/10.1016/j.isprsjprs.2009.04.001.

[27] X. Xiong, A. Adan, B. Akinci, D. Huber, Automatic creation of semantically rich 3D building models from laser scanner data, Autom. Constr. 31 (2013) 325–337, https://doi.org/10.1016/j.autcon.2012.10.006.

[28] R.B. Rusu, N. Blodow, M. Beetz, Fast point feature histograms (FPFH) for 3D registration, in: 2009 IEEE International Conference on Robotics and Automation, IEEE, Kobe, 2009, pp. 3212–3217, https://doi.org/10.1109/ROBOT.2009.5152473.

[29] M. Sharif, M. Nahangi, C. Haas, J. West, Automated model-based finding of 3D objects in cluttered construction point cloud models, Comput. Aided Civ. Inf. Eng. 32 (2017) 893–908, https://doi.org/10.1111/mice.12306.

[30] C. Kim, H. Son, C. Kim, Automated construction progress measurement using a 4D building information model and 3D data, Autom. Constr. 31 (2013) 75–82, https://doi.org/10.1016/j.autcon.2012.11.041.

[31] C. Kim, H. Son, C. Kim, Fully automated registration of 3D data to a 3D CAD model for project progress monitoring, Autom. Constr. 35 (2013) 587–594, https://doi.org/10.1016/j.autcon.2013.01.005.

[32] F. Bosché, Automated recognition of 3D CAD model objects in laser scans and calculation of as-built dimensions for dimensional compliance control in construction, Adv. Eng. Inform. 24 (2010) 107–118, https://doi.org/10.1016/j.aei.2009.08.006.

[33] B. Wang, Q. Wang, J.C.P. Cheng, C. Song, C. Yin, Vision-assisted BIM reconstruction from 3D LiDAR point clouds for MEP scenes, Autom. Constr. 133 (2022) 103997, https://doi.org/10.1016/j.autcon.2021.103997.

[34] Y. Pan, A. Braun, I. Brilakis, Enriching geometric digital twins of buildings with small objects by fusing laser scanning and AI-based image recognition, Autom. Constr. 140 (2022) 104375, https://doi.org/10.1016/j.autcon.2022.104375.

[35] R.Q. Charles, H. Su, M. Kaichun, L.J. Guibas, PointNet: Deep learning on point sets for 3D classification and segmentation, in: 2017 IEEE Conference on Computer Vision and Pattern Recognition (CVPR), IEEE, Honolulu, HI, 2017, pp. 77–85, https://doi.org/10.1109/CVPR.2017.16.

[36] C. Qi, L. Yi, H. Su, L. Guibas, PointNet++: deep hierarchical feature learning on point sets in a metric space, in: Proceedings of the 31st International Conference on Neural Information Processing Systems, Curran Associates Inc., Long Beach, California, USA, 2017, pp. 5105–5114. https://www.scopus.com/inward/record.uri?eid=2-s2.0-85042297004&partnerID=40&md5=accadf2044f1e8592099683263d18d16.

[37] J.W. Ma, T. Czerniawski, F. Leite, Semantic segmentation of point clouds of building interiors with deep learning: augmenting training datasets with synthetic BIM-based point clouds, Autom. Constr. 113 (2020) 103144, https://doi.org/10.1016/j.autcon.2020.103144.

[38] J. Chen, Z. Kira, Y.K. Cho, Deep learning approach to point cloud scene understanding for automated scan to 3D reconstruction, J. Comput. Civ. Eng. 33 (2019) 04019027, https://doi.org/10.1061/(ASCE)CP.1943-5487.0000842.

[39] N. Bolourian, M. Nasrollahi, F. Bahreini, A. Hammad, Point cloud–based concrete surface defect semantic segmentation, J. Comput. Civ. Eng. 37 (2023) 04022056, https://doi.org/10.1061/JCCEE5.CPENG-5009.

[40] C. Yin, B. Wang, V.J.L. Gan, M. Wang, J.C.P. Cheng, Automated semantic segmentation of industrial point clouds using ResPointNet++, Autom. Constr. 130 (2021) 103874 https://doi.org/10.1016/j.autcon.2021.103874.

[41] E. Agapaki, I. Brilakis, CLOI: an automated benchmark framework for generating geometric digital twins of industrial facilities, J. Constr. Eng. Manag. 147 (2021) 04021145, https://doi.org/10.1061/(ASCE)CO.1943-7862.0002171.

[42] X. Yang, E. Del Rey Castillo, Y. Zou, L. Wotherspoon, Y. Tan, Automated semantic segmentation of bridge components from large-scale point clouds using a weighted superpoint graph, Autom. Constr. 142 (2022) 104519, https://doi.org/10.1016/j.autcon.2022.104519.

[43] X. Yang, E. Del Rey Castillo, Y. Zou, L. Wotherspoon, Semantic segmentation of bridge point clouds with a synthetic data augmentation strategy and graph-structured deep metric learning, Autom. Constr. 150 (2023) 104838, https://doi.org/10.1016/j.autcon.2023.104838.

[44] D.H. Ballard, Generalizing the Hough transform to detect arbitrary shapes, Pattern Recogn. 13 (1981) 111–122, https://doi.org/10.1016/0031-3203(81)90009-1.

[45] M. Ester, H.P. Kriegel, J. Sander, X. Xu, A density-based algorithm for discovering clusters in large spatial databases with noise, in: National Conferences on Aritificial Intelligence, 1999. https://www.zhangqiaokeyan.com/academic-conference-foreign_meeting-264296_thesis/0705014483058.html (accessed October 10, 2023).

[46] P.J. Besl, N.D. McKay, A method for registration of 3-D shapes, IEEE Trans. Pattern Anal. Mach. Intell. 14 (1992) 239–256, https://doi.org/10.1109/34.121791.

[47] W. Zhang, G. Tian, C. Yang, Z. Liu, Analytical methods for determining the cable configuration and construction parameters of a suspension bridge, Struct. Eng. Mech. 71 (2019) 603–625, https://doi.org/10.12989/SEM.2019.71.6.603.

Update

Automation in Construction

Corrigendum

Corrigendum to "Automated geometric reconstruction and cable force inference for cable-net structures using 3D point clouds" [Automation in Construction, 165 (2024), 105543]

Siwei Lin [b], Liping Duan [a,b,c], Jiming Liu [b], Xiao Xiao [a,b,c], Ji Miao [b], Jincheng Zhao [a,b,c,*]

[a] State Key Laboratory of Ocean Engineering, School of Ocean and Civil Engineering, Shanghai Jiao Tong University, Shanghai 200240, China
[b] School of Ocean and Civil Engineering, Shanghai Jiao Tong University, Shanghai, China
[c] Shanghai Key Laboratory for Digital Maintenance of Buildings and Infrastructure, Department of Civil Engineering, Shanghai Jiao Tong University, Shanghai, China

The authors apologize for any inconvenience caused by the incorrect data concerning 'Weight' in Table 3 and three ambiguous text descriptions in the original article. The following corrections and clarifications should be made, and the authors confirm that the revision does not influence the results and conclusions in the original article.

1. The weight of connecting members should be updated, see Table 3 below.

Table 3 Design parameters of connecting members.

Position	Width/mm	Height/mm	Length/mm	Weight/kg
#1 / #25	1500.00	1000.00	7550.00	2024.32
#2 / #24	1300.00	1000.00	7550.00	1956.09
#3 / #23	1200.00	1000.00	7550.00	1921.98
#4 / #22	1100.00	1000.00	7550.00	1407.49
#5 / #21	1000.00	1000.00	7550.00	1373.38
#6 / #20	900.00	1000.00	7550.00	1339.27
#7 / #19	800.00	1000.00	7550.00	1298.37
#8 / #18	750.00	1000.00	7550.00	1281.31
#9 / #17	700.00	1000.00	7550.00	1264.26
#10 / #11 / #15 / #16	650.00	1000.00	7550.00	1247.20
#12 / #13 / #14	600.00	1000.00	7550.00	1230.14

2. The last sentence of the first paragraph in Section 4.3.2 should be revised to "Moreover, during the fitting process, it was found that the horizontal deformation is slight, indicating that though the cables were not horizontally braced, the horizontal deformation can be ignored."

3. An introductory paragraph should be added at the beginning of section 4.4 for better understanding.

"In Section 4.3, the set of scans was performed before installing the connecting members, however, as the construction progressed, in Section 4.4, the scan was taken when some of the connecting members were partially installed on the cables. Therefore, in Section 4.4, loads applied to the cables in the cable-net structure consist of the self-weights of cables, cable clamps, and connecting members. The self-weight load of the connecting members is distributed as a concentrated load to the cable clamps at both ends, meaning that each clamp at the ends of the connecting members bears half of the member's self-weight. Specifically, the calculation process for the distributed point forces on the cable is the same as in Section 4.3, except that an additional half of the member's self-weight needs to be added at the position of the cable clamps where the connecting member is installed. On the other hand, the values of concentrated forces applied to the cables can reflect whether the connecting members are installed or not. It should be noted that the installation state of the connecting members during the scanning can be found in Fig. 15. Taking the third cable (6# cable) in Fig. 15 as an example, connecting members are installed on one side of the cable only at the positions of clamps 10#, 13#, and 14#. Taking the 8th cable (11# cable) in Fig. 15 as an example, connecting members are installed on both sides of the cable at the positions of clamps 11#-16#. The installation positions of connecting members on other cables can be inferred similarly. It should be noted that the clamp positions 1#-3# and 23#-25# contain two cable clamps and the self-weight of connecting members can be found in Table 3."

4. The last sentence of the second-to-last paragraph in section 4.4 should be revised to "It should be noted that the force in cable #11 is higher than cable #12 due to the connecting members installed on both sides of cable #11, while cable #12 only has connecting members on one side, resulting in relatively a smaller cable force. The numbers 1-9 in Figure 15 are only for the convenience of labelling the cable force for each cable."

The authors would like to apologize for any inconvenience caused.